



## Nano-engineering of three-dimensional core/shell nanotube arrays for high performance supercapacitors

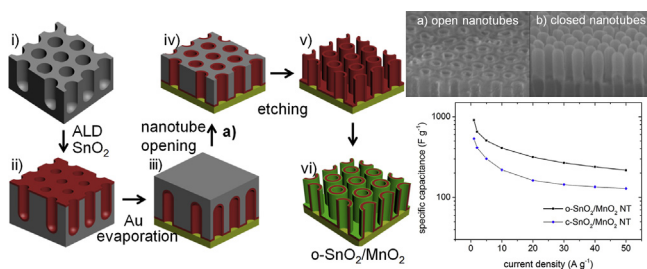
Fabian Grote, Liaoyong Wen, Yong Lei\*

Technical University of Ilmenau, Institute of Physics & IMN MacroNano® (ZIK), Prof. Schmidt-Str. 26, 98693 Ilmenau, Germany

### HIGHLIGHTS

- Free-standing three-dimensional  $\text{SnO}_2/\text{MnO}_2$  core/shell nanotubes.
- Demonstration of an innovative template-based fabrication technique with high structural controllability.
- Novel strategy to selectively fabricate open-end and closed-end nanotubes.
- Excellent electrochemical performance compared to other  $\text{MnO}_2$ -based nanostructures.
- High specific capacitance  $910 \text{ F g}^{-1}$  at  $1 \text{ A g}^{-1}$  and a good rate capability.

### GRAPHICAL ABSTRACT



### ARTICLE INFO

#### Article history:

Received 18 November 2013

Received in revised form

4 December 2013

Accepted 6 December 2013

Available online 17 January 2014

#### Keywords:

Template nano-fabrication

Anodic aluminum oxide

Three-dimensional

Core/shell nanotube

Atomic layer deposition

Supercapacitors

### ABSTRACT

Large-scale arrays of core/shell nanostructures are highly desirable to enhance the performance of supercapacitors. Here we demonstrate an innovative template-based fabrication technique with high structural controllability, which is capable of synthesizing well-ordered three-dimensional arrays of  $\text{SnO}_2/\text{MnO}_2$  core/shell nanotubes for electrochemical energy storage in supercapacitor applications. The  $\text{SnO}_2$  core is fabricated by atomic layer deposition and provides a highly electrical conductive matrix. Subsequently a thin  $\text{MnO}_2$  shell is coated by electrochemical deposition onto the  $\text{SnO}_2$  core, which guarantees a short ion diffusion length within the shell. The core/shell structure shows an excellent electrochemical performance with a high specific capacitance of  $910 \text{ F g}^{-1}$  at  $1 \text{ A g}^{-1}$  and a good rate capability of remaining  $217 \text{ F g}^{-1}$  at  $50 \text{ A g}^{-1}$ . These results shall pave the way to realize aqueous based asymmetric supercapacitors with high specific power and high specific energy.

© 2013 Elsevier B.V. All rights reserved.

### 1. Introduction

Energy storage and energy management are one of the key challenges of mankind in this century in order to meet the requirement of an increasing intermittent energy supply. The demand of energy storage systems include small storage systems for energy harvesting applications [1], medium size applications such

as energy storage systems for electrical mobility [2], and large scale systems leveling peaks in power grids [3]. In all these applications supercapacitors play a crucial role and are discussed as a desirable solution to address these emerging challenges. In the past decade various approaches have been attempted to increase the performance of supercapacitors. First, severe effort was made to increasing the electrode surface area by reducing the surface morphology into the nanometer regime and fabricating nanostructured electrodes [4–6]. And second, new electrode materials, such as activated carbons [7,8], and pseudocapacitive materials including conductive polymers [9–11] and metal oxides [4,12–15]

\* Corresponding author. Tel.: +49 3677 69 3748.

E-mail address: [yong.lei@tu-ilmenau.de](mailto:yong.lei@tu-ilmenau.de) (Y. Lei).

were introduced. [6,16–18] So far two major challenges in the field of supercapacitors exist: (i) highly promising supercapacitor materials such as  $\text{MnO}_2$  suffer from high internal resistance ( $\sim 10^2$ – $10^6 \Omega \text{ cm}^{-1}$ ), which limits the electrochemical performance in supercapacitor devices; (ii) it is important to realize a high controllability of all structural parameters to optimize the electrochemical properties of supercapacitors, so as to identify the ideal configuration of high performance devices. In order to solve these challenges, novel functional nanostructures and material compositions (and related fabrication processes) need to be developed. An attractive solution is offered by preparing large-scale arrays of one-dimensional (1D) core/shell nanostructures including nanowires and nanotubes. Such nano-engineered materials combine the unique properties of two materials (*i.e.*, core and shell). Usually, the highly conductive core provides a fast electron transport through the entire electrode and the thin shell ensures a well utilization of the energy storage material and a short ion diffusion. Template-based techniques are efficient methods to prepare large-arrays of 1D nanostructures [19–23], especially for core/shell structures [24,25]. However, the level of controllability of the template-based techniques is partially limited to a few parameters and largely depends on the inherent structural nature of the template itself. Atomic layer deposition (ALD), as an efficient process to prepare conformal films or tubular structures, provides a good solution to further adjust more structural parameters.

Here, we demonstrate an innovative technique to realize highly ordered free-standing three-dimensional (3D) arrays of  $\text{SnO}_2/\text{MnO}_2$  core/shell nanotubes with precise controllability of many structural parameters. This includes not only diameter, spacing, and length of the core/shell nanostructures originated from the template fabrication process, but also the wall thickness of the core and shell nanotubes. Moreover, advanced core/shell nanostructures including open-end and closed-end nanotubes (denoted as o- for open-end and c- for closed-end nanotubes) are achieved, so as to investigate and optimize the electrochemical mechanism for supercapacitor applications. Very importantly, based on the property optimization of the 3D core/shell nanostructures, we obtained an electrochemical performance that is among the highest reported values for  $\text{MnO}_2$ -based nanostructures.

## 2. Experimental section

### 2.1. Preparation

Porous anodic aluminum oxide nano-templates were fabricated using a two-step anodization process from 99.999% pure aluminum foils with a second anodization time of 5–15 min followed by a pore widening process in a 5 wt%  $\text{H}_3\text{PO}_4$  solution for 15 min [26,27]. Such templates were used for the growth of the  $\text{SnO}_2$  nanotube arrays by a PicoSun ALD system according to the following procedure. The reaction chamber was heated to 250 °C, and  $\text{SnCl}_4$  and  $\text{H}_2\text{O}$  were selected as the precursors. First  $\text{SnCl}_4$  precursor was pulsed for 1 s and purged for 4 s, followed by a 2 s pulse and 8 s purge of  $\text{H}_2\text{O}$ . This procedure was repeated for 500–1500 times depending on the desired wall thickness of  $\text{SnO}_2$  nanotubes. After this process, a 100 nm thick layer of gold was evaporated onto the sample by physical vapor deposition to support the  $\text{SnO}_2$  nanotube array. Afterward the remaining Al was removed by a saturated solution of  $\text{CuCl}_2$ . In the next step, the template was removed. Hereby different processes for open-end and closed-end nanotube arrays were used. For the fabrication of closed-end nanotubes the entire templates was removed in a 5 wt%  $\text{NaOH}$  solution for 120 min. In order to successfully fabricate open-end  $\text{SnO}_2$  nanotubes, the templates were first partially etched for 20 min to only liberate the nanotubes top parts. Then the top-ends of the nanotubes were removed by

scratching the surface with a sharp scalpel. Thereafter the sample was placed again in a 5 wt%  $\text{NaOH}$  solution to remove the remaining template. Finally the  $\text{SnO}_2$  nanotube array was attached to a stainless steel holder.

The as-prepared open-end and closed-end  $\text{SnO}_2$  nanotube arrays were coated by  $\text{MnO}_2$  shells. A thin  $\text{MnO}_2$  layer was formed by electrochemical deposition in an electrolyte containing 0.1 M  $\text{Mn}(\text{Ac})_2$  and 0.1 M  $\text{Na}_2\text{SO}_4$ , using 1 V versus a  $\text{Ag}/\text{AgCl}$  reference electrode. A Pt foil was used as a counter electrode. The charge passed was controlled during the deposition process within the range of 130–260 mC. Afterward the samples were cleaned with water and dried.

The entire fabrication process with all steps is shown schematically in the supplementary video.

Supplementary data related to this article can be found online at <http://dx.doi.org/10.1016/j.jpowsour.2013.12.029>.

### 2.2. Electrochemical and physical characterizations

All electrochemical measurements were performed in a three electrode cell with a 1 M  $\text{Na}_2\text{SO}_4$  electrolyte, an  $\text{Ag}/\text{AgCl}$  reference electrode, and a Pt foils as the counter electrode. The CV and charge/discharge curves were measured from 0 to 0.9 V vs  $\text{Ag}/\text{AgCl}$  at scan rates of 2, 5, 10, 20, and 50 mV s<sup>-1</sup> and current densities of 1, 2, 5, 10, 20, 30, 40, 50 A g<sup>-1</sup>, respectively. The EIS was performed at 0.1 V with a 10 mV pulse in the frequency range of 100 kHz–0.05 Hz. All measurements were performed on a Bio-Logic VSP electrochemical work station.

The structural characterization was carried out using SEM (Hitachi S-4800) and TEM (Libra 200 FE).

X-ray photoelectron spectroscopy (XPS) was performed under an emission angle of 53° using a monochromated  $\text{AlK}\alpha$  source and a hemispherical electron analyzer.

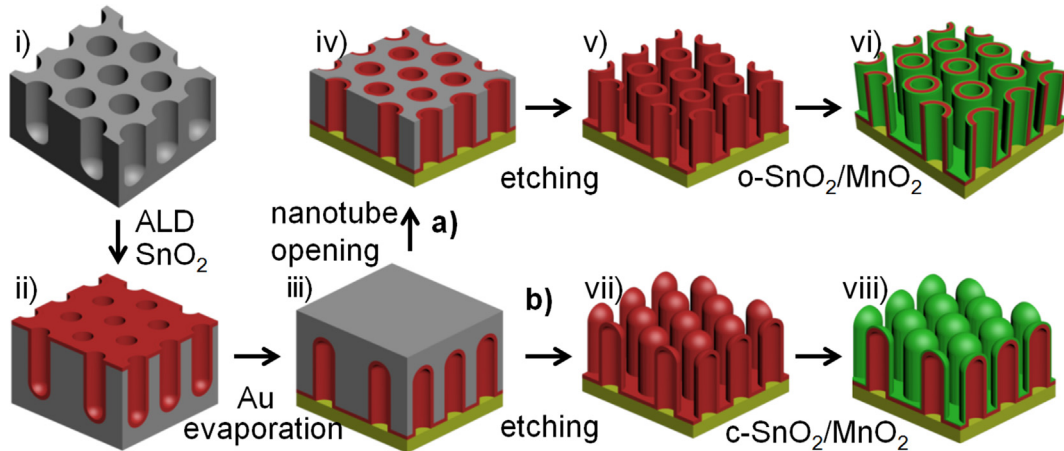
## 3. Results and discussion

### 3.1. Characterization of the $\text{SnO}_2/\text{MnO}_2$ core/shell nanotube array

The fabricated  $\text{SnO}_2/\text{MnO}_2$  core/shell nanotube arrays are prepared by the ALD process of  $\text{SnO}_2$  into a porous anodic aluminum oxide nano-template and a subsequent conformal coating by  $\text{MnO}_2$ , as illustrated in [Scheme 1](#). Thereby it is possible to selectively control the synthesis of o- $\text{SnO}_2/\text{MnO}_2$  (process a in [Scheme 1](#)) and c- $\text{SnO}_2/\text{MnO}_2$  core/shell nanotubes (process b in [Scheme 1](#)). This selectivity is a salient feature of the fabrication process and highly desirable for supercapacitor applications. The possibility of fabricating open-end nanotube arrays enables the access of the total inner and outer surface area of a nanotube for charge storage and thus is superior to closed-end nanotube arrays, which possess a lower accessible surface area.

The morphology of the prepared  $\text{SnO}_2$  core nanotubes is analyzed by scanning electron microscopy (SEM) and transmission electron microscopy (TEM), as shown in [Fig. 1](#). The SEM image in [Fig. 1a](#) clearly shows a highly ordered free-standing array of o- $\text{SnO}_2$  nanotubes (for c- $\text{SnO}_2$  nanotubes see [Fig. S1](#)). The outer diameter and the inter-tube distance of the nanotubes are about 60 nm and 105 nm respectively, which are inherited from the structural parameters of the templates. Different lengths of nanotubes between 600 nm and 1800 nm are obtained by using templates with different thicknesses, indicating that the length of nanotubes can be tuned by the template thickness.

The opening process of the  $\text{SnO}_2$  nanotubes is shown in [Fig. 2](#). First, the anodic aluminum oxide nano-template is partially etched to liberate the closed nanotube top-ends. Then the liberated closed nanotube top-ends are removed by scratching the samples surface



**Scheme 1.** Illustration of the fabrication processes of a) open-end o-SnO<sub>2</sub>/MnO<sub>2</sub> nanotube arrays and b) closed-end c-SnO<sub>2</sub>/MnO<sub>2</sub> nanotube arrays. i) Starting from porous anodic aluminum oxide nano-template, ii) conformal coating of template with SnO<sub>2</sub> by atomic layer deposition, iii) turning sample and fabrication of current collector by e-beam evaporation of gold; process a): iv) partial etching of porous anodic aluminum nano-template and nanotube opening by scratching process, v) removing of template to gain highly ordered free-standing SnO<sub>2</sub> nanotube array, vi) electrochemical coating with MnO<sub>2</sub>; process b): vii) complete removing of template, viii) electrochemical coating with MnO<sub>2</sub>.

with a sharp scalpel, resulting in open-end nanotubes (please refer to the supplementary video). The wall thickness and the inner diameter of the SnO<sub>2</sub> nanotubes are investigated by TEM measurements (Fig. 1c). The wall thickness of about 8 nm is evaluated from the contrast profile in the inset of Fig. 1c (using the similar method as described in Ref. [28]). It depends on the total cycle number during the ALD fabrication process and the growth rate, which is estimated to be approximately 0.08 Å/cycle. It is found that 8 nm is an optimal trade-off of wall thickness to maximize the overall inner surface area (*i.e.*, enlarge the inner-tube diameter) and in the same time to keep high mechanical stability of the SnO<sub>2</sub> nanotubes (*i.e.*, thicken the tube walls). Therefore, for the

nanotubes with about 60 nm outer diameter, 105 nm inter-tube distance and 8 nm tube thickness, the inner diameter and the inter-tube spacing are about 44 nm and 45 nm, respectively. Hence there are sufficient inner- and outer-tube spaces for the next step of conformal coating of MnO<sub>2</sub>.

Subsequently the SnO<sub>2</sub> nanotubes are conformal coated by MnO<sub>2</sub> in an electrochemical deposition process. The formed MnO<sub>2</sub> shell layer is investigated by TEM and SEM measurements. Fig. 3a shows a TEM image of a single SnO<sub>2</sub> nanotube covered entirely by a thin layer (10–20 nm thickness) of MnO<sub>2</sub>. The elemental distribution across the SnO<sub>2</sub>/MnO<sub>2</sub> nanotube is investigated by EDX line scan and verifies the presents of Sn, Mn, and O. The elemental distribution of Sn shows two peaks located at the wall positions of the nanotube, whereas Mn is distributed more uniformly across the nanotube (this might originates from the fact that MnO<sub>2</sub> was coated on both the inner and outer surfaces of SnO<sub>2</sub> tubes). The SEM image in Fig. 3b shows that the SnO<sub>2</sub> nanotubes are covered completely by MnO<sub>2</sub>. The difference between the MnO<sub>2</sub>-coated nanotubes and uncoated bare SnO<sub>2</sub> nanotubes is presented clearly in Fig. 3b. The coated nanotubes possess much rougher surfaces comparing to uncoated tubes, which is a typical results of electrochemical deposited MnO<sub>2</sub>. Well conformal coating of MnO<sub>2</sub> on SnO<sub>2</sub> nanotubes can only be achieved by using optimized fabrication

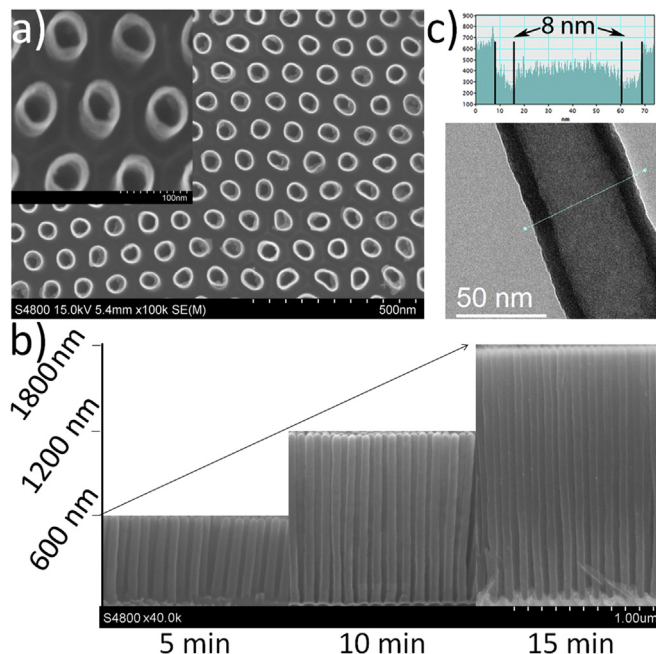


**Fig. 1.** a) Top view SEM image of an o-SnO<sub>2</sub> nanotube array. The inset shows the inter-tube distance  $d_{int} = 105$  nm and inter-tube spacing  $d_{spac} = 44$  nm b) cross-section SEM image showing the length of the nanotubes in dependence of the template anodization time (*i.e.*, thickness of the template). c) TEM image, showing the hollow nature of the nanotubes. The inset shows the contrast profile across the nanotube and reveals a wall thickness of around 8 nm.

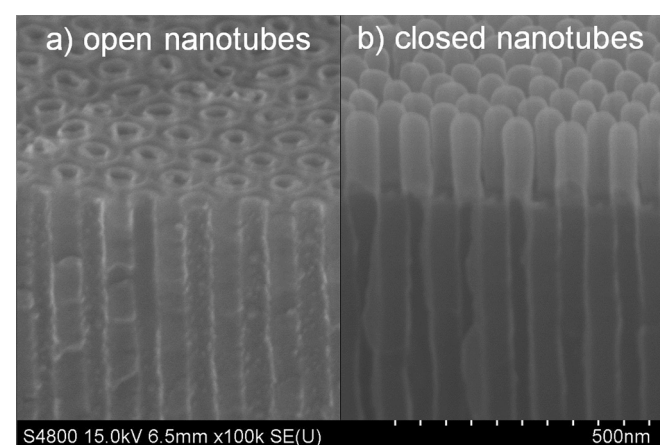


**Fig. 2.** a) Open nanotube array after removing the closed top-ends of the nanotubes by scratching the surface with a sharp scalpel; b) partially etched nanotube array showing the liberated closed top-ends before removing.

conditions and controlling the amount of material being deposited (an excessive deposition of  $\text{MnO}_2$  is leading to an in-conformal coating as shown in Fig. S2). Finally an optimal window of 130–260 mC flown charge in electrochemical deposition is determined for well conformal coating of  $\text{MnO}_2$ .

### 3.2. Electrochemical performance

The electrochemical performance of the prepared core/shell nanostructures is investigated in a three-electrode setup. The measuring cell includes a platinum foil as a counter electrode, an  $\text{Ag}/\text{AgCl}$  reference electrode and a water-based electrolyte containing 1.0 M  $\text{Na}_2\text{SO}_4$ . Fig. 4a shows the cyclovoltammetry (CV) curves of o- $\text{SnO}_2/\text{MnO}_2$  nanotube arrays. All CV scans were performed in a potential range from 0 to 0.9 V vs  $\text{Ag}/\text{AgCl}$  at scan rates of 2, 5, 10, 20, and 50  $\text{mV s}^{-1}$  and show scaling behavior of the current as the scan rate is increased. The shape of the CV curves reassembles the expected shape for pseudocapacitive charge storage in  $\text{MnO}_2$  and indicates good capacitance behavior of our sample. During a standard cycle voltammetry testing, Mn undergoes redox reactions on the surface of samples ( $\text{MnO}_2$  shell in our case). Thereby the valance state of Mn shall be reduced in the charging process and increased in the discharging process. This process is caused by the intercalation/deintercalation of protons ( $\text{H}^+$ ) or alkali cations ( $\text{Na}^+$ ) into/out of the  $\text{MnO}_2$  shell. This reaction can be described as [29]:



Galvanostatic charge/discharge curves of as-prepared o- $\text{SnO}_2/\text{MnO}_2$  nanotube array are recorded at different current densities to evaluate the specific capacitance and rate capability, as shown in Fig. 4b. The specific capacitance is calculated for various current densities from the associated discharge curve according to the following equation:

$$c = I / \left( \frac{\Delta V}{\Delta t} \times m \right) \quad (3)$$

with  $c$  ( $\text{F g}^{-1}$ ),  $I$  (A),  $\Delta V/\Delta t$  ( $\text{V s}^{-1}$ ), and  $m$  (g) being the specific capacitance, discharge current, gradient of discharge curve

obtained by dividing the width of the potential window (i.e., 0.9 V) by the discharge time, and mass of the active material, respectively. It is noteworthy that the gained specific capacitance of the core/shell structures can be attributed to the charge storage capability of the  $\text{MnO}_2$  shell. [30] This assumption is justified because the  $\text{SnO}_2$  nanotubes are conformally covered by  $\text{MnO}_2$  during the shell formation and therefore can rarely contribute to the charge storing capability because the charges are stored near or at the surface of the electrode. [30] Moreover, in the *Supplementary information* we discussed the possible influence of the  $\text{SnO}_2$  on the electrodes performance. The graph in Fig. 4d displays the obtained specific capacitance at different current densities and compares the rate capability of o- $\text{SnO}_2/\text{MnO}_2$  and c- $\text{SnO}_2/\text{MnO}_2$  core/shell nanotubes. It can be seen that the o- $\text{SnO}_2/\text{MnO}_2$  nanotube array exhibits an extremely high specific capacitance of 910  $\text{F g}^{-1}$  at 1  $\text{A g}^{-1}$  and remains a high specific capacitance of 217  $\text{F g}^{-1}$  at 50  $\text{A g}^{-1}$ . As shown in Fig. 5, this performance outnumbers the performance of pure nanostructured  $\text{MnO}_2$  electrodes. And very importantly, it is among the highest reported values of  $\text{MnO}_2$ -based core/shell nanostructures. Beyond that the prepared core/shell structure exhibits a high areal capacitance of up to 0.092  $\text{F cm}^{-2}$  at 1  $\text{A g}^{-1}$  and 0.022  $\text{F cm}^{-2}$  at 50  $\text{A g}^{-1}$ , which is higher than reported values of other core/shell structures [31]. In addition the reported structure obtains a high volumetric capacitance of 511  $\text{F cm}^{-3}$  at 1  $\text{A g}^{-1}$  and 122  $\text{F cm}^{-3}$  at 50  $\text{A g}^{-1}$ . The performance of the c- $\text{SnO}_2/\text{MnO}_2$  nanotube arrays remains behind the values achieved by o- $\text{SnO}_2/\text{MnO}_2$  nanotube arrays at same mass loadings, as presented in Figs. 4d and 5. It is believed that this difference could be attributed to the lower available surface area of c- $\text{SnO}_2$  electrodes and a longer ion diffusion length. It clearly shows that a highly porous open-end nanotube structure as a core material is superior to core materials based on closed-end nanotubes and nanowires.

The investigation of the long-time cycling stability of the o- $\text{SnO}_2/\text{MnO}_2$  nanotube array is shown in Fig. 4c. The electrode is consecutively charged and discharged for 2600 cycles at 5  $\text{A g}^{-1}$ . The electrode capacitance decreases during the first 100 charge/discharge cycles. Thereafter the charge/discharge profile is constant for 2500 cycles, which is confirmed by the charge/discharge curves in the inset of Fig. 4c. This result demonstrates that the o- $\text{SnO}_2/\text{MnO}_2$  nanotube arrays are capable of accomplishing thousands of charge/discharge cycles and are ideal candidates for long-time applications.

The electrochemical performance of the o- $\text{SnO}_2/\text{MnO}_2$  nanotube array is further investigated by electrochemical impedance spectroscopy, as shown in the Nyquist plot in Fig. S4. The impedance plot is composed of a steep line in the low frequency region and a semi-circle in the high frequency region. The almost vertical line in the low frequency region reveals the good capacitive behavior of the electrode material due to fast and reversible reactions occurring at or near the surface of the electrode. The high frequency region gives evidence about the equivalent series resistance ( $R_s$ ) at the low x-axis interception and about the charge transfer resistance ( $R_{ct}$ ) at the interception at ( $R_s + R_{ct}$ ) [32]. The equivalent series resistance and the charge transfer resistance of the o- $\text{SnO}_2/\text{MnO}_2$  nanotube array are measured to be 2.09  $\Omega$  and 1.53  $\Omega$ , respectively, and are lower or comparable to other reported core/shell structures [33,34]. In contrast, electrodes consisting of pure  $\text{MnO}_2$  generally show higher resistance values due to the high internal resistance of  $\text{MnO}_2$ . For comparison, the electrochemical impedance spectrum obtained from a thin  $\text{MnO}_2$  layer on a gold substrate with same mass loading shows remarkably higher charge-transfer resistance compared to the core/shell structure, see Fig. S4. These results obtained from EIS indicate that the o- $\text{SnO}_2/\text{MnO}_2$  core/shell structure with its conductive core and thin shell is a favorable

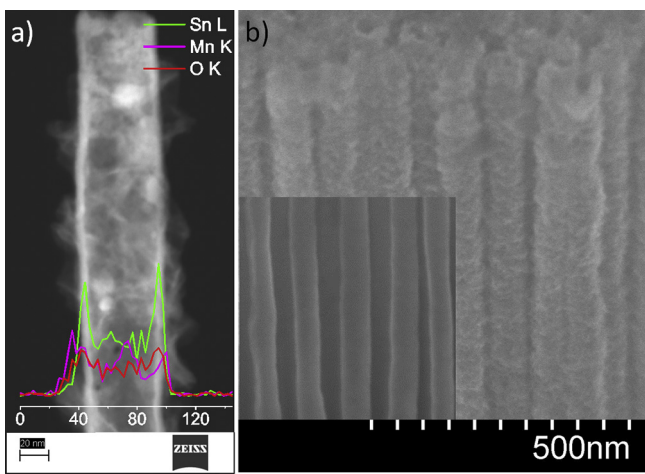


**Fig. 3.** Morphology of o- $\text{SnO}_2/\text{MnO}_2$  core/shell nanotube. a) Cross-section TEM image with EDX line scan showing the elemental distribution of Mn, Sn, and O across a single core/shell nanotube. b) SEM image of  $\text{MnO}_2$ -coated  $\text{SnO}_2$  nanotubes compared with bare  $\text{SnO}_2$  nanotubes shown in the inset. Scale bar is valid for both images.

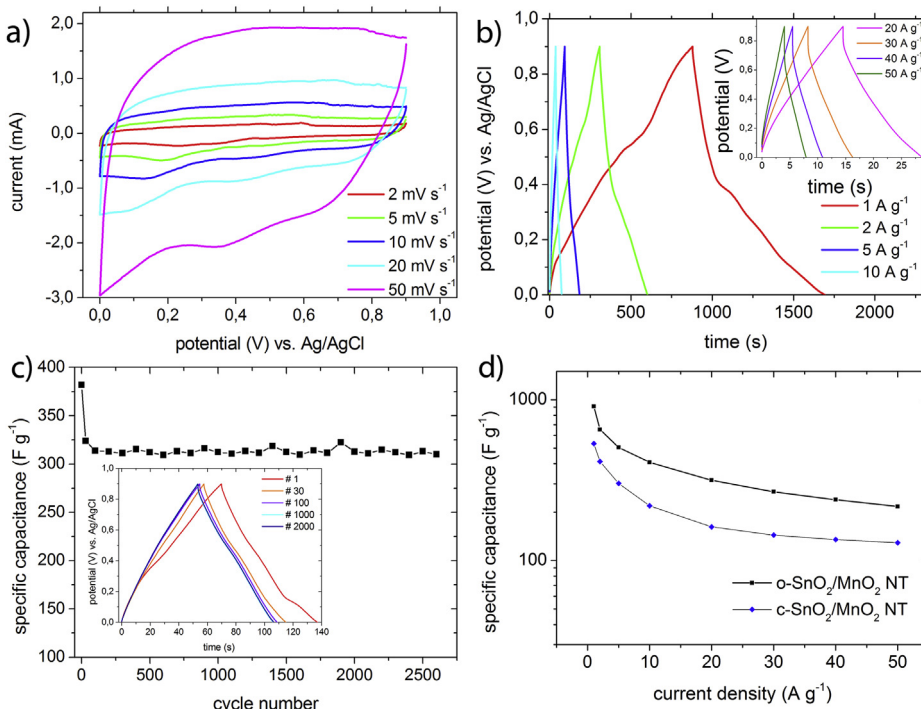


**Fig. 4.** Electrochemical performance of the o-SnO<sub>2</sub>/MnO<sub>2</sub> core/shell nanotube array with a nanotube length of 1.8  $\mu\text{m}$ . a) CV curves at different current densities, b) charge/discharge profiles at different current densities, c) long-time cycling stability at 5  $\text{A g}^{-1}$  including various charge/discharge curves in the inset, d) rate capability of o-SnO<sub>2</sub>/MnO<sub>2</sub> and c-SnO<sub>2</sub>/MnO<sub>2</sub> nanotube arrays.

electrode structure to enhance the electrochemical performance and rate capability of supercapacitors.

#### 4. Conclusion

In summary, a nano-engineering strategy for fabricating SnO<sub>2</sub>/MnO<sub>2</sub> core/shell nanotube arrays is innovated in this work. The fabrication process allows precise controlling of the length, spacing, diameter, wall thickness and the selection of open-end or closed-

end nature of the prepared nanotubes. The synthesized structures exhibit excellent electrochemical performances with an outstanding rate capability, which shows that these well-defined nanostructures are good candidates for positive supercapacitor electrodes in applications that require micro-supercapacitors such as consumer electronics, wireless sensor network, and energy harvesting devices. It should be noted that the presented fabrication process can be applied to many other materials and applications.

#### Acknowledgments

We kindly acknowledge the help of M. Himmerlich and S. Kirschok (TU Ilmenau) for XPS measurements and M. Peterlechner and G. Wilde (University of Münster) for TEM measurements. Financial support from the European Research Council Grant (ThreeDSurface) and BMBF (ZIK: 3DNanoDevice) is gratefully acknowledged.

#### Appendix A. Supplementary data

Supplementary data related to this article can be found at <http://dx.doi.org/10.1016/j.jpowsour.2013.12.029>.

#### References

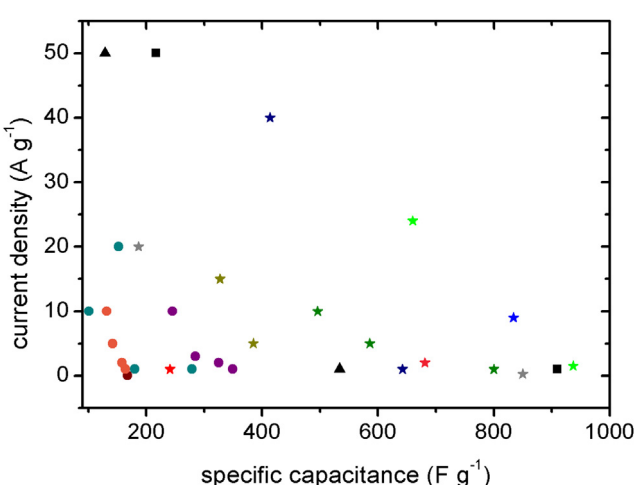


**Fig. 5.** Values of specific capacitance and current density for various reported MnO<sub>2</sub> based structures (circles: pure MnO<sub>2</sub>, stars: core/shell material), including the data of this work: ■ o-SnO<sub>2</sub>/MnO<sub>2</sub>, ▲ c-SnO<sub>2</sub>/MnO<sub>2</sub>, ★ MnO<sub>2</sub>/Mn [35], ★ MnO<sub>2</sub>/TiN [31], ★ MnO<sub>2</sub>/TiN [34], ★ MnO<sub>2</sub>/SnO<sub>2</sub> [28], ★ MnO<sub>2</sub>/Zn<sub>2</sub>SnO<sub>4</sub> [33], ★ MnO<sub>2</sub>/Au [36], ★ MnO<sub>2</sub>/Ni [37], ★ MnO<sub>2</sub>/aMEGO [38], ● MnO<sub>2</sub> NT [39], ● MnO<sub>2</sub> NW [14], ● MnO<sub>2</sub> NW [40], ● CNT/MnO<sub>2</sub> [41].

- [1] F.I. Simjee, P.H. Chou, IEEE Trans. Power Electron. 23 (2008) 1526–1536.
- [2] J.R. Miller, P. Simon, Science 321 (2008) 651–652.
- [3] Siemens, [w3.siemens.com/smartgrid/global/en/products-systems-solutions/rail-electrification/dc-traction-power-supply/pages/mobile-energy-storage.aspx](http://w3.siemens.com/smartgrid/global/en/products-systems-solutions/rail-electrification/dc-traction-power-supply/pages/mobile-energy-storage.aspx), 2013.
- [4] C.-C. Hu, K.-H. Chang, M.-C. Lin, Y.-T. Wu, Nano Lett. 6 (2006) 2690–2695.
- [5] A.L.M. Reddy, S.R. Gowda, M.M. Shajumon, P.M. Ajayan, Adv. Mater. 24 (2012) 5045–5064.
- [6] A.S. Arico, P. Bruce, B. Scrosati, J.-M. Tarascon, W. van Schalkwijk, Nat. Mater. 4 (2005) 366–377.

[7] M.G. Hahm, A. Leela Mohana Reddy, D.P. Cole, M. Rivera, J.A. Vento, J. Nam, H.Y. Jung, Y.L. Kim, N.T. Narayanan, D.P. Hashim, C. Galande, Y.J. Jung, M. Bundy, S. Karna, P.M. Ajayan, R. Vajtai, *Nano Lett.* (2012) 5616–5621.

[8] D. Pech, M. Brunet, H. Durou, P. Huang, V. Mochalin, Y. Gogotsi, P.-L. Taberna, P. Simon, *Nat. Nanotechnol.* 5 (2010) 651–654.

[9] M. Mastragostino, C. Arbizzani, F. Soavi, *Solid State Ionics* 148 (2002) 493–498.

[10] M.E. Roberts, D.R. Wheeler, B.B. McKenzie, B.C. Bunker, *J. Mater. Chem.* 19 (2009) 6977–6979.

[11] K. Naoi, M. Morita, *Electrochem. Soc. Interface* 17 (2008) 44–48.

[12] J.-K. Chang, W.-T. Tsai, *J. Electrochem. Soc.* 150 (2003) A1333–A1338.

[13] V. Subramanian, H. Zhu, R. Vajtai, P.M. Ajayan, B. Wei, *J. Phys. Chem. B* 109 (2005) 20207–20214.

[14] H. Jiang, T. Zhao, J. Ma, C. Yan, C. Li, *Chem. Commun.* 47 (2011) 1264–1266.

[15] X. Tang, H. Li, Z.-H. Liu, Z. Yang, Z. Wang, *J. Power Sources* 196 (2011) 855–859.

[16] B.E. Conway, *Electrochemical Supercapacitors: Scientific Fundamentals and Technological Applications*, Plenum Press, 1999.

[17] B.E. Conway, V. Birss, J. Wojtowicz, *J. Power Sources* 66 (1997) 1–14.

[18] P. Simon, Y. Gogotsi, *Nat. Mater.* 7 (2008) 845–854.

[19] Y. Lei, K.-S. Yeong, J.T.L. Thong, W.-K. Chim, *Chem. Mater.* 16 (2004) 2757–2761.

[20] Y. Lei, W. Cai, G. Wilde *Prog. Mater Sci.* 52 (2007) 465–539.

[21] Y. Lei, Z. Jiao, M. Wu, G. Wilde, *Adv. Eng. Mater.* 9 (2007) 343–348.

[22] S. Yang, Y. Lei, *Nanoscale* 3 (2011) 2768–2782.

[23] M. Daub, M. Knez, U. Gosele, K. Nielsch, *J. Appl. Phys.* 101 (2007).

[24] Z.-L. Wang, R. Guo, L.-X. Ding, Y.-X. Tong, G.-R. Li, *Sci. Rep.* 3 (2013).

[25] J. Liu, J. Jiang, M. Bosman, H.J. Fan, *J. Mater. Chem.* 22 (2012) 2419–2426.

[26] H. Masuda, K. Fukuda, *Science* 268 (1995) 1466–1468.

[27] Y. Lei, S. Yang, M. Wu, G. Wilde, *Chem. Soc. Rev.* 40 (2011) 1247–1258.

[28] I. Perez, E. Robertson, P. Banerjee, L. Henn-Lecordier, S.J. Son, S.B. Lee, G.W. Rubloff, *Small* 4 (2008) 1223–1232.

[29] M. Toupin, T. Brousse, D. Belanger, *Chem. Mater.* 16 (2004) 3184–3190.

[30] J. Yan, E. Khoo, A. Sumboja, P. See Lee, *ACS Nano* 4 (2010) 4247–4255.

[31] S.A. Sherrill, J. Duay, Z. Gui, P. Banerjee, G.W. Rubloff, S.B. Lee, *Phys. Chem. Chem. Phys.* 13 (2011) 15221–15226.

[32] B.Y. Chang, S.M. Park, in: E.S. Yeung, R.N. Zare (Eds.), *Annu. Rev. Anal. Chem.*, 2010, pp. 207–229.

[33] L. Bao, J. Zang, X. Li, *Nano Lett.* 11 (2011) 1215–1220.

[34] S. Dong, X. Chen, L. Gu, X. Zhou, L. Li, Z. Liu, P. Han, H. Xu, J. Yao, H. Wang, X. Zhang, C. Shang, G. Cui, L. Chen, *Energy Environ. Sci.* 4 (2011) 3502–3508.

[35] Q. Li, Z.-L. Wang, G.-R. Li, R. Guo, L.-X. Ding, Y.-X. Tong, *Nano Lett.* 12 (2012) 3803–3807.

[36] L.G. Xue, H. Hao, Z. Wei, T. Huang, A.S. Yu, *J. Solid State Electrochem.* 15 (2011) 485–491.

[37] D.L. Yan, Z.L. Guo, G.S. Zhu, Z.Z. Yu, H.R. Xu, A.B. Yu, *J. Power Sources* 199 (2012) 409–412.

[38] X. Zhao, L. Zhang, S. Murali, M.D. Stoller, Q. Zhang, Y. Zhu, R.S. Ruoff, *ACS Nano* 6 (2012) 5404–5412.

[39] H. Xia, J. Feng, H. Wang, M.O. Lai, L. Lu, *J. Power Sources* 195 (2010) 4410–4413.

[40] S.-L. Chou, J.-Z. Wang, S.-Y. Chew, H.-K. Liu, S.-X. Dou, *Electrochem. Commun.* 10 (2008) 1724–1727.

[41] X. Wei, X. Hui, Y.H.F. Jerry, L. Li, *Phys. Scr.* (2010) 014008.